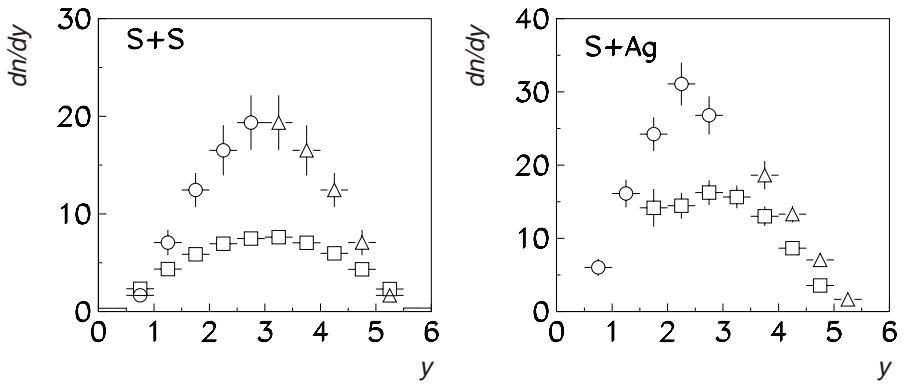

Fig. 9.1. The abundance of $1.6\Lambda + 4\mathrm{K_S} + 1.6\overline{\Lambda}$ as a function of rapidity. On the left, S–S; on the right, S–Ag (open circles are the directly measured data). The triangles are reflected data points for S–S and reflected interpolated data employing S–S and S–Ag. The squares in the S–S case are the results for N–N collisions scaled up by the pion-multiplicity ratio; for S–Ag these are the scaled-up p–S results. Data courtesy of the NA35 collaboration [128].

9 Highlights of hadron production

9.1 The production of strangeness

Strangeness is a valuable tool for understanding the reaction mechanism, since it has to be made during the collision. The question is that of how it is produced. In terms of experimental information, the first thing we would like to establish is whether the mechanism producing strangeness involves a hot fireball at central rapidity, or whether perhaps a lot of strangeness originates from the projectile/target-fragmentation region.

Results of the experiment NA35 [128] are shown in Fig. 9.1 as functions of rapidity for the case of S–S 200A-GeV collisions. We consider the overall abundance of $\langle \mathrm{s} + \bar{\mathrm{s}} \rangle$. The open circles are the measured data points, the open triangles are the symmetrically reflected data points, and squares on the left-hand side are the results of N–N (isospin-symmetric nucleon–nucleon) collisions scaled up by the ratio in pion multiplicity, whereas on the right-hand side the p–S results are scaled up. We show the rapidity yield obtained by integrating the transverse-mass $m_\perp$ distribution for the total yield of strangeness:

$$\frac{d\langle \mathrm{s} + \bar{\mathrm{s}} \rangle}{dy} = 1.6\,\frac{d\Lambda}{dy} + 4\,\frac{d\mathrm{K_S}}{dy} + 1.6\,\frac{d\overline{\Lambda}}{dy}. \tag{9.1}$$

We note that, on doubling the $\mathrm{K_S}$ yield, we include $\mathrm{K_L}$, and, on doubling again, we add both $\mathrm{K^+}$ and $\mathrm{K^-}$, which explains the factor 4.

https://doi.org/10.1017/9781009290753.013 Published online by Cambridge University Press

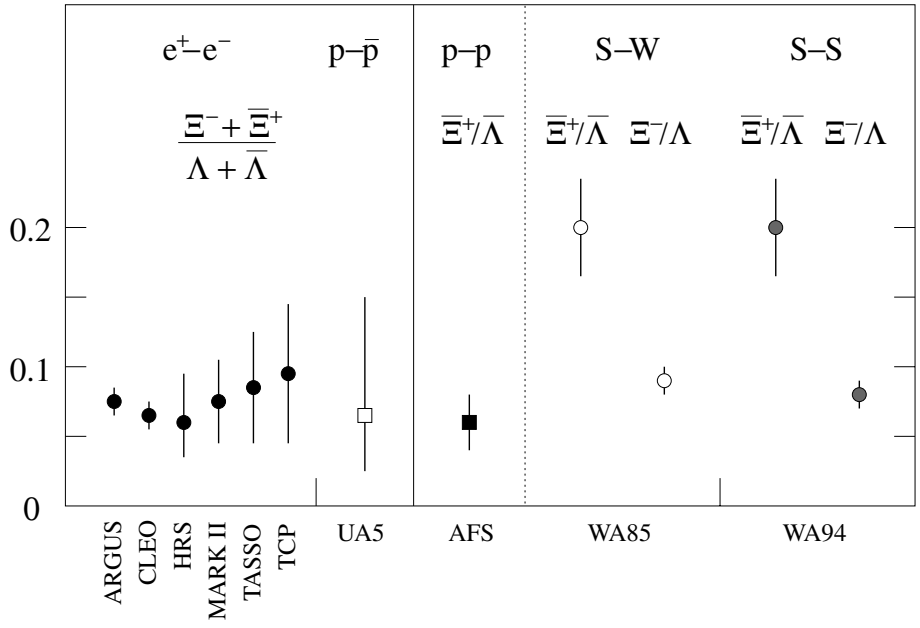

Fig. 9.2. The ratio (at fixed $p_\perp$) of (multi)strange baryon–antibaryon particle abundances, measured in the central rapidity region for 200A-GeV S–S/W collisions, compared with ratios obtained in lepton- and nucleon-induced reactions. Data assembled by the WA85/94 collaboration [1–5, 7].

In Fig. 2.6 on page 32, we saw that a factor 1.5 allows one to extrapolate the yields of Λ and $\overline{\Lambda}$ to include all singly strange hyperons. However, there is also strong production of multistrange Ξ and $\overline{\Xi}$, with $\Xi^-/\Lambda \simeq 0.1$ and $\overline{\Xi}^+/\overline{\Lambda} \simeq 0.2$, as is seen in Fig. 9.2. Assuming similar rapidity distributions for Ξ^- and Λ and $\overline{\Xi}^+$ and $\overline{\Lambda}$, and remembering that, for each charged Ξ, there is its neutral isospin partner, this implies that the coefficient of Λ should have been 1.9, and that of $\overline{\Lambda}$ 2.3, in order to account for the production of multistrange hyperons. Thus the enhancement in production of strange particles seen in Fig. 9.1 is slightly (by $\simeq 6\%$) understated.

The difference between scaled N–N and S–S data is most pronounced at central rapidity ($y_{\rm CM} = 2.97$), and it disappears within one unit of the projectile- and target-fragmentation regions. At central rapidity $y \simeq 3$, a new source of strangeness not present in the N–N-collision system contributes. The S–S system is relatively small, thus stopping is small, and it is quite impressive that the enhancement in production of strangeness is observed only at central rapidity. Since other SPS experiments involved heavier nuclei and/or lower energy, and thus certainly involved more stop-

https://doi.org/10.1017/9781009290753.013 Published online by Cambridge University Press

ping, we can be sure that the excess of strangeness at the SPS originates at central rapidity.

We show, in the right-hand panel of Fig. 9.1, similar results for S–Ag collisions: the open circles are the measured points, open triangles are estimates based on S–S and the 'reflected' S–Ag results, and the open squares are pion-multiplicity-scaled p–S results. An enhancement in production of strangeness is also seen here, though the asymmetry of the collision system makes it more difficult to understand the effect quantitatively.

The abundant strangeness, in the central rapidity region, is at the origin of the effective production of multistrange antibaryons. The WA85 and WA94 collaborations [1–5, 7] explored the relative abundances at central rapidity of the various strange baryons and antibaryons produced in S–W and S–S reactions. The central-rapidity particle ratios have been obtained at $p_\perp \geq 1\,\mathrm{GeV}$. The results for relative abundances are reported when yields of particles of unequal masses are compared, both with $p_\perp \geq 1$ GeV and using as cutoff a fixed value of $m_\perp \geq 1.7\,\mathrm{GeV}$. The results at fixed $p_\perp$ are shown in Fig. 9.2. In the left-hand panel, we see the annihilation and production results from e^+–e^- and p–$\bar{p}$ reactions, in the middle panel, we see the ISR–AFS p–p measurement of $\overline{\Xi}/\overline{\Lambda}$, which is a factor of five below the S–W and S–S result, even though the ISR energy $\sqrt{s_{\mathrm{NN}}}$ was nearly four times higher than is available at the SPS. In S–S and S–W interactions a clear enhancement of the $\overline{\Xi}^+/\overline{\Lambda}$ ratio is observed, which has been predicted as a signature of the QGP [215, 226].

A more extreme picture of the enhancement is found when we compare the yields of various hyperons at fixed $m_\perp$, as would be done in a thermal model considering coalescence of quarks to give hadrons. This means that, on comparing, e.g., $\overline{\Xi}$ with $\overline{\Lambda}$, we are looking at particles at different $p_\perp$. The experimental results reported by the WA85 collaboration, for S–W interactions at $200A$ GeV, are at 'fixed $m_\perp$':

$$\left.\frac{\overline{\Xi^-}}{\overline{\Lambda}+\overline{\Sigma^0}}\right|_{m_\perp} = 0.4 \pm 0.04\,, \qquad \left.\frac{\Xi^-}{\Lambda+\Sigma^0}\right|_{m_\perp} = 0.19 \pm 0.01. \tag{9.2}$$

We introduce the average singly strange hyperon yield Y(qqs), which at fixed $m_\perp$ is the same for all components:

$$\mathrm{Y} = \Lambda = \Sigma^0 = \Sigma^+ = \Sigma^-. \tag{9.3}$$

Thus, the actual antihadron ratio is indeed twice as large as that measured:

$$\left.\frac{\overline{\Xi^-}}{\overline{\mathrm{Y}}}\right|_{m_\perp} \simeq 0.8 \pm 0.1\,. \tag{9.4}$$

https://doi.org/10.1017/9781009290753.013 Published online by Cambridge University Press

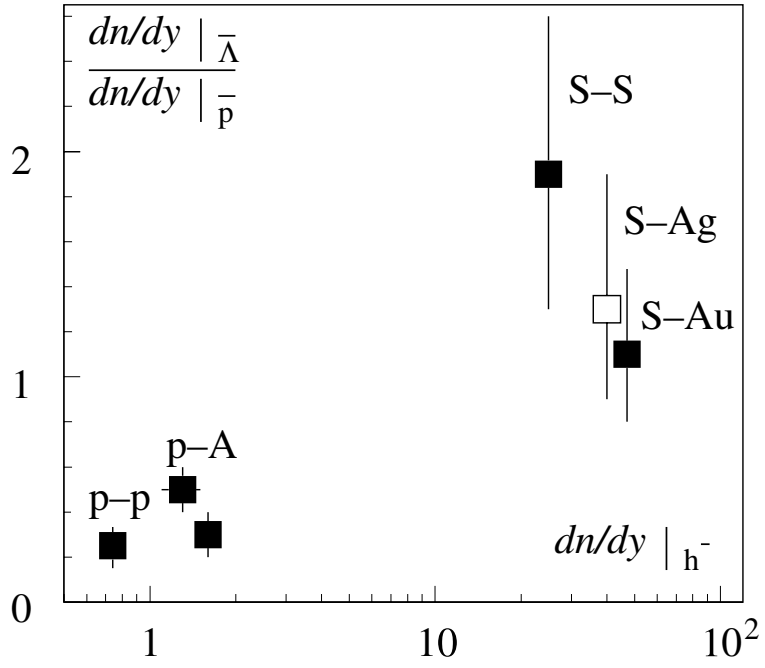

Fig. 9.3. The ratio of the rapidity density dn/dy for $\overline{\Lambda}/\bar{\mathrm{p}}$, measured at central y, as a function of the negative-hadron central-rapidity density $dn/dy|_{\mathrm{h}^-}$. NA35 collaboration [46, 47, 138].

We now consider the quark content:

$$\left.\frac{\overline{\Xi}}{\overline{\Upsilon}}\right|_{m_\perp} = \left.\frac{\bar{\mathrm{s}}\bar{\mathrm{s}}\bar{\mathrm{q}}}{\bar{\mathrm{s}}\bar{\mathrm{q}}\bar{\mathrm{q}}}\right|_{m_\perp} = \left.\frac{\bar{\mathrm{s}}}{\bar{\mathrm{q}}}\right|_{m_\perp} \simeq 0.8. \tag{9.5}$$

We see that, at the time of production of antihyperons, there has been comparable availability of antiquarks at high momentum, $\bar{\mathrm{u}} = \bar{\mathrm{d}} = 1.2\bar{\mathrm{s}}$. This result is hard to explain other than in terms of QGP, for which, at the values of statistical parameters applicable here, near to chemical equilibrium all three antiquark flavors are at nearly equal abundances. Since the abundance of light quarks comprises valence quarks, it is twice as large, as can be seen in Fig. 10.3 on page 203, $\mathrm{u} = \mathrm{d} \simeq 2.5\mathrm{s}$, consistent with the half as large baryon ratio seen on the right-hand side of Eq. (9.2). These results involving the abundances of multistrange antibaryons have not been explained in terms of hadron-cascade models.

Consistent with this result is the observation of the NA35 collaboration [24, 25, 54] regarding the $\overline{\Lambda}/\bar{\mathrm{p}}$ ratio. In Fig. 9.3, we show this ratio as a function of the negative-hadron rapidity density $dn/dy|_{\mathrm{h}^-}$ at central y. The p–p and p–A reactions are at small values of $dn/dy|_{\mathrm{h}^-}$, whereas

https://doi.org/10.1017/9781009290753.013 Published online by Cambridge University Press

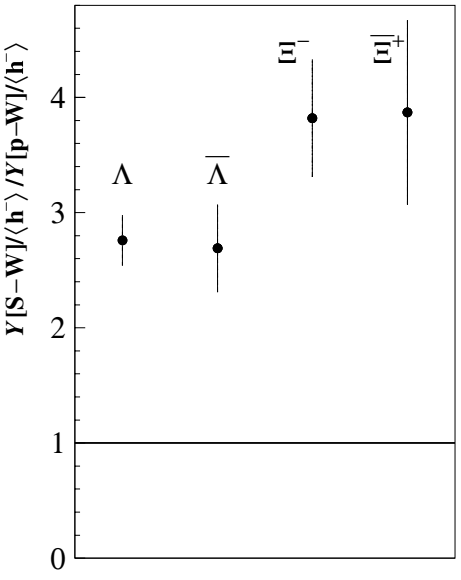

Fig. 9.4. Ratios of abundances of particles (Λ, $\overline{\Lambda}$, Ξ and $\overline{\Xi}$) normalized with respect to the abundance of h^-: S–W results divided by p–W results at 200A GeV in the rapidity window $2.5 < y < 3$ for 1.4 GeV/$c < p_\perp < 3$ GeV/c. WA85 collaboration [41].

the S–S, S–Ag, and S–Au reactions are accompanied by a relatively high $dn/dy|_{h^-}$. We observe that there is an increase in this ratio by nearly a factor five, and, even more significantly, the abundance of the *heavier* and *strange* $\overline{\Lambda}$ is similar to if not greater than the abundance of $\bar{p}$.

The enhancement in production of strange hyperons and antihyperons can be studied by comparing it directly with the yield seen in p–A interactions. For this purpose, one obtains specific yields of strange particles 'sp', normalized with respect to the yield of negative hadrons h^-. These can be compared with such yields in proton-induced interactions, i.e., we look at the enhancement E_s^i in production of a strange particle i defined as

$$E_s^i \equiv \frac{Y_{sp}^i(\text{S–A})}{Y_{sp}^i(\text{p–A})}, \tag{9.6}$$

where $i = (\Lambda, \overline{\Lambda}, \Xi, \overline{\Xi})$. The results are presented in Fig. 9.4 [41]. We see an enhancement of this specific yield in nuclear interactions, compared with p–A collisions, and this enhancement increases with increasing strangeness content. The stronger enhancement in production of multistrange hadrons is expected for hadronization involving enhancements in yield and density of strangeness compared with p–A interactions.

https://doi.org/10.1017/9781009290753.013 Published online by Cambridge University Press

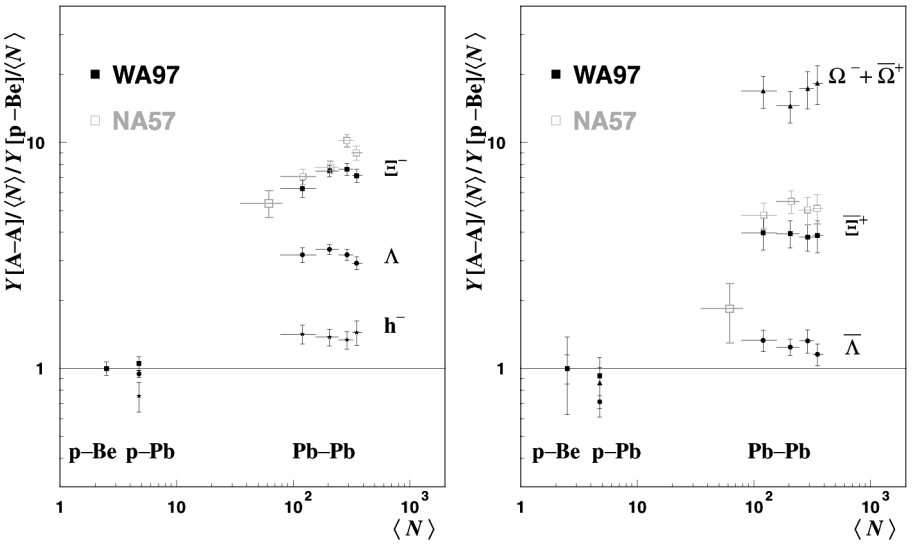

Fig. 9.5. Yields Y per wounded nucleon $\langle N \rangle$ in Pb–Pb relative to p–Be collisions from WA97 [41] (solid data points), and from NA57 for Ξ^- and $\overline{\Xi}^-$ [108] (open data points).

This presentation of enhancement in production of strange hadrons understates the magnitude of the effect since it is diluted by the overall enhancement of the yield of h^-, which is also expected to arise due to the enhancement of entropy in QGP, see section 7.1. Therefore a method to extrapolate the yields from p–A interactions to A–A interactions was devised, by scaling with the number of participating (wounded) nucleons $\langle N \rangle$ [41]. The Pb–Pb 158A GeV results of the WA97 collaboration are shown in Fig. 9.5, using the p–Be interaction results as reference. Solid points are the four centrality bins considered. We have presented some of these results in Fig. 1.6 on page 19. The absolute enhancement in production of strange particles compared to the p–Be extrapolated yields increases strongly with the strangeness content.

In order to understand whether there is a threshold for the enhancement to occur, the experiment NA57 has repeated the measurement of the experiment WA97, and has extended the reach by studying more peripheral collisions. In the most peripheral fifth data bin the number of participants is 60. At this time, only the Ξ^- and $\overline{\Xi}^-$ NA57 data for Pb–Pb are available, as is seen in Fig. 9.5. The rapid drop in enhancement of the production of $\overline{\Xi}^-$ is most remarkable, and, if it is confirmed in, e.g., $\overline{\Omega}$ results, this can be seen as definitive evidence for a rather sudden onset of the formation of QGP as a function of the size of the system.

https://doi.org/10.1017/9781009290753.013 Published online by Cambridge University Press

We do not yet have a similar measurement for the onset of the enhancement as a function of energy. The specific production of strangeness per hadron is shown in Fig. 1.5 on page 17. However, there is a rapid change in hadron yield with energy, thus this result, as we have discussed in section 1.6, is not fully representative of the energy dependence of strangeness production. Another complication with the study of the energy dependence is the presence of the energy threshold for antibaryon production. Thus the energy dependence of the enhancement in production of strange antibaryons has to be evaluated, not with reference to the p–A reaction system, but entirely within the A–A system. The low-energy measurement, presumably under pre-QGP conditions, can be used to establish a basis against which the production at higher energy can be studied. In such a measurement, we can hope and expect to see a sudden onset with energy of the yield of multistrange (anti)baryons, if indeed a new state of matter is being created.

Another important topic in the production of strange hadrons, is the symmetry of particle and antiparticle spectra seen in Fig. 1.7 on page 20. As discussed, see table 8.2, the fitted inverse-slope parameters agree at the level of 1%, when statistics is good enough: $T^{\Lambda} = 289 \pm 3$ MeV, to be compared with $T^{\overline{\Lambda}} = 287 \pm 4$ MeV [42]. There is no evidence for any difference at small momenta, for which the annihilation reaction would be most significant. Thus we can literally 'see', in Fig. 1.7, that these particles are escaping from the central fireball without further interaction with hadronic gas.

9.2 Hadron abundances

Despite the relative smallness of the S–S collision system, and the highest available fixed-target heavy-ion energy, the remarkable difference between Λ and $\overline{\Lambda}$ rapidity distributions, shown in Fig. 8.4, proves that neither is the baryon-punch-through Bjørken reaction picture applicable, nor do we see stopping of the valence quarks in the central region, as we discussed in section 8.3. How does the situation look for nonstrange hadrons? In Fig. 9.6, we see the rapidity distribution of negative particles h^-, which comprise π^-, K^-, and $\bar{p}$, shown per collision event for the 5% most central Pb–Pb 158A-GeV collisions (full triangles), 3% most central S–S 200A-GeV collisions (stars, multiplied by factor 6.5), and the N–N interactions (full dots, multiplied by a factor 176) [43]. Detailed study of the chemical composition of hadrons produced in these experiments, section 19.3, leads to an estimate that the π^- make up 92% of these particles, K^- make up 6.6%, and $\bar{p}$ contribute 1.1% in Pb–Pb fixed target interactions at 159A GeV.

https://doi.org/10.1017/9781009290753.013 Published online by Cambridge University Press

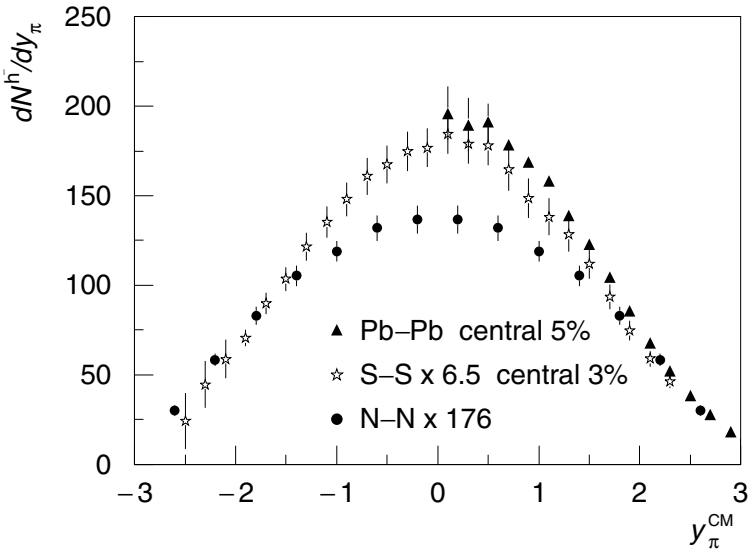

Fig. 9.6. The pseudorapidity distribution of negative hadrons (sum of π^-, K^- and $\bar{p}$) in Pb–Pb, scaled S–S, and N–N collisions [43].

The abundance of h^- produced in the Pb–Pb reactions can be obtained from Fig. 9.6. On fitting the h^- distribution to a Gaussian shape,

$$\frac{dn}{d\eta} = n_0 e^{-(y-y_{\rm CM})^2/\Gamma}, \qquad \frac{\sigma^2}{2} = \Gamma, \tag{9.7}$$

one finds $\sigma \simeq 1.4$ (half width at half maximum). The integral of the distribution gives the total multiplicity of all negative hadrons, after an additional minor correction [43]: $\langle h^- \rangle = 695 \pm 30$. Thus, in geometrically central Pb–Pb 158A-GeV interactions, the total hadron multiplicity is nearly 2400 per event, when we allow for positively charged and neutral hadrons. Since the maximum negative-hadron abundance at $y = 0$ is $dh^-/dy|_{\rm max} \simeq 200$, we also have $dn_{\rm h}/dy|_{\rm max} \simeq 680$ in these events.

To compare with Pb–Pb data, the S–S yields have been scaled up by a factor 6.5, this factor arising from the ratio of participants, which are in Pb–Pb measured to be 352 ± 12, and in S–S 52 ± 3. A further factor 0.96 is introduced by the NA49 collaboration to account for the difference in collision energy, which is somewhat higher in the S–S system. However, no correction for the fact that S–S is proton–neutron symmetric and Pb–Pb asymmetric was made. This correction may be significant since π^- is the carrier of the excess in valence d quarks, and there are 80 more d–$\bar{\rm d}$ present than u–$\bar{\rm u}$. Given that $\langle h^- \rangle \simeq 700$, an enrichment of π^- by valence quarks of projectile and target could reach a non-negligible level of 10%.

https://doi.org/10.1017/9781009290753.013 Published online by Cambridge University Press

Were this 'isospin' correction introduced, it would perhaps be difficult to distinguish the Pb–Pb from S–S results in Fig. 9.6, and both are notably greater than the N–N-based expectations: the observed yields have been scaled by the factor 176 which is the ratio of Pb–Pb to N–N participants. We conclude that, both in Pb–Pb and in S–S collisions, we observe a similar per participant central rapidity excess in hadron multiplicity, and thus also an excess in production of entropy; see chapter 7.

The relevance of the 40% excess in production of h^- in A–A collisions at SPS energies is amplified by the opposite behavior seen at the lower AGS energies, for which there is a 20% suppression compared with the scaled nucleon–nucleon results. One can qualitatively argue about the AGS result obtained at much lower energies as follows: whereas in N–N reactions all pions produced reach the detectors, pions produced in a series of N–N collisions at the AGS are deposited in dense baryonic matter, where some can be absorbed. Moreover, a notable amount of the available collision energy is used to do work to compress colliding nuclear matter, and this energy is not available to produce pions, a point already noted in early work with relativistic heavy ions [233]. We will not pursue the implications of the suppression of pion production at fixed-target collision energies below $15A$ GeV, for the study of the nuclear-matter equations of state.

Since there is a change in pattern of behavior of pion production as a function of the collision energy, we consider in a more systematic way whether this can be understood in terms of a general change in pattern of behavior as a function of collision energy. Gaździcki [126] proposed to explore this effect as a function of the Fermi-energy variable [121, 172, 174]

$$F \equiv \frac{(\sqrt{s_{\mathrm{NN}}} - 2m_{\mathrm{N}})^{3/4}}{(\sqrt{s_{\mathrm{NN}}})^{1/4}}, \tag{9.8}$$

where $\sqrt{s_{\mathrm{NN}}}$ is the CM energy for a nucleon–nucleon pair and m_{N} is the nucleon mass. There are several advantages in using F as an energy variable. The measured mean multiplicity of pions in N–N interactions is approximately proportional to F [127]. In the Landau model [172, 174], both the entropy and the initial temperature of the matter (for $\sqrt{s_{\mathrm{NN}}} \gg 2m_{\mathrm{N}}$) are also proportional to F.

In Fig. 9.7, we see the average yield of all pions $\langle\pi\rangle$ per average participating nucleon $\langle \mathrm{N_p}\rangle$. The data is from [127], with the most recent results presented in [254]. The lower straight line follows open diamonds, which are results from N-N interactions, whereas the upper line follows the high-energy SPS (squares) and RHIC (open crosses) results. The cross over from the one behavior to the other is seen at the lower range of SPS energies, whereas the AGS results (triangles) indeed fall below the

https://doi.org/10.1017/9781009290753.013 Published online by Cambridge University Press

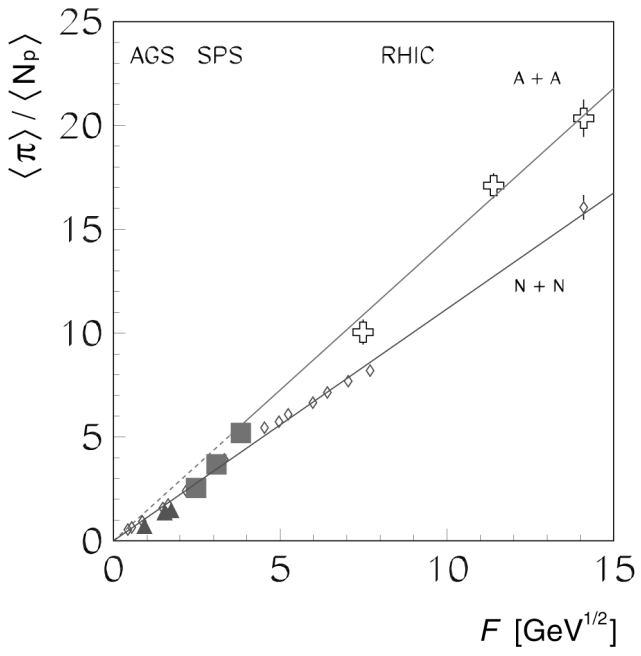

Fig. 9.7. The per-participant average yield of pions $\langle\pi\rangle/\langle N_p\rangle$ as a function of the Fermi-energy variable F, results from A–A and N–N interactions.

N–N results. Both high-energy SPS and RHIC results are seen to follow the 'high-entropy' branch (see chapter 7), which differs clearly from the low-entropy reactions at the AGS and in N–N collisions.

Not only the yield of pions harbors a mystery. The shape of the SPS rapidity distribution for hadrons, see Fig. 9.6, is not fully understood today, and we can not convincingly explain why there is so little difference in shape among the three reactions shown. Generally, one would expect the h^- yield in S–S reactions to be 'wider' in rapidity than that for Pb–Pb collisions. Instead, what we see in Fig. 9.6 is that the rapidity shape of h^- produced in N–N reactions is the same as that observed in Pb–Pb reactions, apart from an additional central-rapidity contribution. However, we recall the qualitative study seen in Fig. 8.5, along with the observation that about half of all pions observed are actually decay products of hadronic resonances. The dilemma in understanding this distribution is in fact one of the reasons that encourages us to focus on the study of particle spectra that are fully made of newly created matter, such as $\overline{\Lambda}$, see Fig. 8.4. These are clearly a more sensitive, and less model-dependent, probe of novel physics occurring in the central rapidity region.

https://doi.org/10.1017/9781009290753.013 Published online by Cambridge University Press

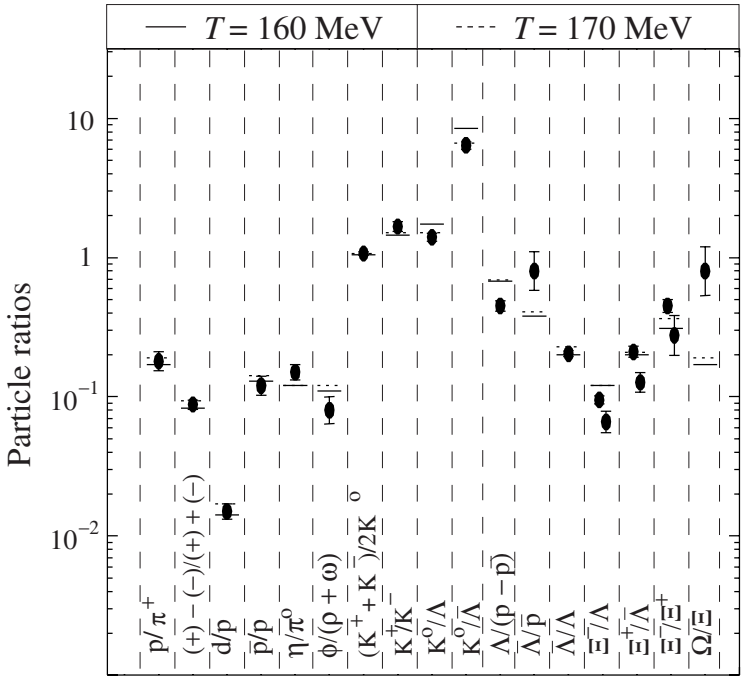

Fig. 9.8. Particle ratios (experimental dots) seen in A–A 200A-GeV reactions for various particle species (shown in horizontal order), compared with the prediction of the thermal model for two different freeze-out temperatures and quark fugacity $\lambda_q = 1.42$ [82].

Further below, we will return to consider, in Fig. 9.19, the rapidity distribution of all charged hadrons observed at the nearly eight-fold higher RHIC energy. There is some spreading of the distribution, which need not be entirely due to the rapidity-versus-pseudorapidity effect we discussed in Fig. 8.3, originating most probably from the expected onset of transparency and outflow of baryon number from the central region.

The spectra of many identified hadronic particles have been measured over sufficiently large ranges of rapidity and transverse mass to allow extrapolation to cover all of the relevant kinematic domain, and the total particle-production yield can be established. The total yields of particles are not dependent on the deformation of the spectra arising from the collective flow motion within the source. Consideration of relative abundance ratios eliminates biases from the various experimental set-ups, in particular the event trigger bias cancels out.

We show the compilation of CERN (200A-GeV) and AGS (14A-GeV) data in Figs. 9.8 and 9.9, in a procedure in which chemical-yield equilibrium of hadron abundances is assumed in a statistical model. In some

https://doi.org/10.1017/9781009290753.013 Published online by Cambridge University Press

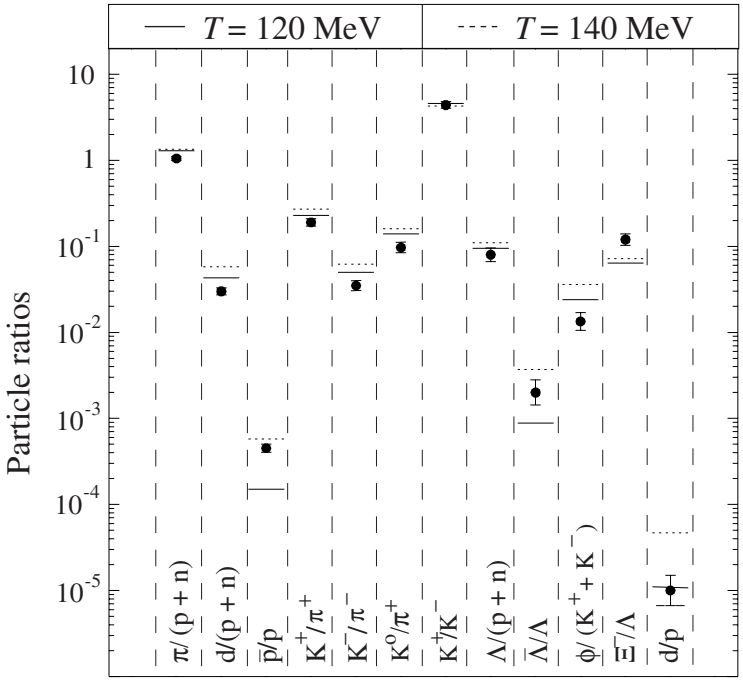

Fig. 9.9. Particle ratios seen in A–A 14A-GeV reactions (solid lines) for various particle species compared with the prediction of the thermal model for two different freeze-out temperatures and quark fugacity $\lambda_q = 4$ [82].

cases seen in these figures, the experimental errors are smaller than the size of the experimental 'dot'.

We see that the particle ratios span typically several decades, yet the systematic pattern of theoretical and experimental results coincides. Thus, the production of hadronic particles occurs, without doubt, near to the chemical equilibrium. We note that the two chemical freeze-out (particle-production) source temperatures used were $T = 160$ and 170 MeV for 200A-GeV data and $T = 120$ and 140 MeV for the AGS 14A-GeV results. Other parameters used in Figs. 9.8 and 9.9 include, for 200-GeV data, the quark fugacity $\lambda_q = 1.42$ and, for 14-GeV data, $\lambda_q = 4$. Conservation of strangeness is imposed as a constraint, i.e., the number of strange quarks and antistrange quarks, in different hadrons, balances exactly. We will discuss how to perform this calculation in chapter 11.

The first impression we have is that we see a rather good systematic agreement in the behavior of the particle yields with this statistical equilibrium-abundance model: almost all gross features of the data, for both sets, are well reproduced. Before we proceed, let us therefore pause to wonder if we should abandon the kinetic, i.e., collisional theory

https://doi.org/10.1017/9781009290753.013 Published online by Cambridge University Press

of particle production, and focus solely on the experimental fact that the observed hadronic multiplicities are the result of a preestablished statistical distribution, which works so well. In a sense, this finding confirms a 15 year-old prediction that such a result can be naturally explained in terms of a dynamic theory of a transient deconfined state hadronizing in a coalescence model [166]. Only a detailed study of the subtle deviations in hadron yields from precise statistical equilibrium yields allows one to understand the hadronization mechanism [69], and therefore ultimately also to explore the properties of the hadronizing QGP state.

Indeed, looking closer at Figures 9.8 and 9.9, we see systematic deviations involving, in particular, (multi)strange particles: in the 200A-GeV data the yield anomalies mostly involve strange antibaryons. The net deviations in the total hadron yields are in fact greater – for example, were the chemical freeze-out condition set to reproduce, in the 200A-GeV case, the ratio $\Lambda/(\mathrm{p}-\bar{\mathrm{p}})$ exactly, we would have enhanced the disagreement in the ratio $\overline{\Lambda}/\bar{\mathrm{p}}$ further. There is clear evidence, in these two figures, that yields of strange particles require greater attention, beyond chemical-equilibrium mode, and we devote much of our effort in this book to understanding the physics behind this phenomenon.

Figures 9.8 and 9.9 demonstrate that the yields of strange antibaryons compared to non-strange hadrons in general vary between 50%–150% of the chemical-equilibrium yield. This strangeness 'fine structure' yield variation is one of the reasons that the measurement of abundances of rarely produced (strange)antibaryons is an excellent diagnostic tool in the study of the properties of the dense hadronic matter, as we have discussed above and in section 2.2. For this reason, we will discuss the production of strangeness and strange antibaryons as signature of QGP in considerably more detail in part VI.

9.3 Measurement of the size of a dense-matter fireball

An important aspect of hadron-production studies is the measurement of two-particle Bose–Einstein correlations, which permits one to evaluate the size of the space–time region. Also Fermi–Dirac correlations can be considered, but practical considerations have favored the measurement of the positive-boson interference. The two-particle intensity interferometry originates from the ambiguity in the path between the source and the detector for indistinguishable quantum particles. The two-particle intensity method was developed by Hanburry-Brown and Twiss as means of determining the dimensions of distant astronomical objects, and is referred to in short hand as 'HBT'; see [75] and references therein.

HBT analysis is today a wide subject of specialization, which could fill this book. We will briefly introduce the method of analysis and present

https://doi.org/10.1017/9781009290753.013 Published online by Cambridge University Press

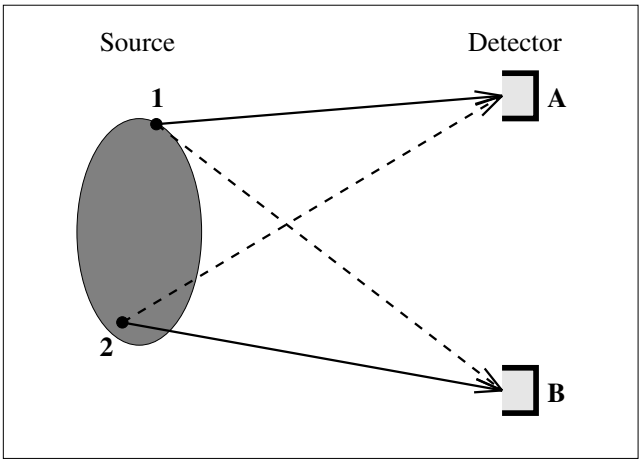

Fig. 9.10. HBT interference: detectors A and B see quantum waves emitted from different source locations 1 and 2 differently.

some recent results. In Fig. 9.10, we illustrate an uncorrelated source of particles π_1 and π_2, with momentum p_1 and p_2, emitted from some points 1 and 2, respectively, within an emission region (the shadowed region in Fig. 9.10). Particles are counted at points A and B. When two observed quantum particles are identical, two indistinguishable histories are possible, drawn with full and dashed lines, respectively, in Fig. 9.10.

The intensity-interference pattern is observed as an enhancement in the number of like-particle (boson) pairs originating from a single source, normalized with respect to a random sample of particles from two different interactions. This enhancement is studied by means of the two-particle correlation function,

$$C_2(p_\mathrm{A}, p_\mathrm{B}) = \frac{\rho(\mathrm{A},\mathrm{B})}{\rho(\mathrm{A}) * \rho(\mathrm{B})}, \tag{9.9}$$

where the numerator represents events with particles registering in both detectors, and the denominator the number of pairs of uncorrelated particles. If no correlation in particle intensity exists, the counts in both detectors are independent, which means that $\rho(\mathrm{A},\mathrm{B}) \to \rho(\mathrm{A}) * \rho(\mathrm{B})$.

The correlation function is in principle dependent on the momenta of both particles observed. A first simple measure of the size of the source is obtained by considering C_2 for similar transverse momenta of both particles. Summing over all other variables ('projecting'), one finds that, as a function of the difference in transverse momenta $\vec{q}_\perp = \vec{p}_{\mathrm{A},\perp} - \vec{p}_{\mathrm{B},\perp}$, $C_2(p_\mathrm{A}, p_\mathrm{B})$ exhibits a clear correlation peak near $q_\perp = 0$.

More generally, the shape of the enhancement as a function of the available momentum variables contains information on the geometric source

https://doi.org/10.1017/9781009290753.013 Published online by Cambridge University Press

parameters and thus both the size and the shape of the source, and, when models are considered, also its dynamic evolution. The difference in momentum for pions $\vec{q} = \vec{p}_{\mathrm{A}} - \vec{p}_{\mathrm{B}}$, can be decomposed using as a reference vector the sum of the pion momenta (the pair momentum) $\vec{p} = \vec{p}_{\mathrm{A}} + \vec{p}_{\mathrm{B}}$, as well as the collision axis of nuclei. The 'longitudinal' direction 'l' with corresponding difference in momentum q_{l} is also referred to as the 'beam' direction, as is appropriate for fixed-target experiments.

The 'out' component of the transverse-momentum-difference vector $\vec{q}_{\perp}$ (as before, transverse with respect to the beam axis) is the projection onto the pion-momentum axis of $\vec{q}_{\perp}$:

$$q_{\mathrm{o}} = \frac{\vec{q}_{\perp} \cdot \vec{p}_{\perp}}{|\vec{p}_{\perp}|}. \tag{9.10}$$

The 'side' component q_{s} is the remaining second component of $\vec{q}_{\perp}$ and its magnitude is

$$q_{\mathrm{s}} = \sqrt{\vec{q}_{\perp}^{\,2} - q_{\mathrm{o}}^2}. \tag{9.11}$$

In the fits of the correlation functions, one likes to sharpen the definition of the longitudinal (beam) component, considering that $\vec{p}$ is in general not normal to the axis,

$$q_{\mathrm{l}}^2 = q_z^2 - q_{\mathrm{o}}^2 + \frac{p_{\mathrm{o}} q_{\mathrm{o}} - p_z q_z}{p_{\mathrm{o}}^2 - p_z^2}, \tag{9.12}$$

where q_z is the magnitude of the difference in momenta for the pair along the longitudinal (beam) axis, and p_z is the same component of the sum of momenta of the pair.

The correlation C_2 is fitted to the form comprising three source-shape parameters R_i:

$$C_2 = D\Big(1 + \lambda e^{-(q_{\mathrm{o}}^2 R_{\mathrm{o}}^2 + q_{\mathrm{s}}^2 R_{\mathrm{s}}^2 + q_{\mathrm{l}}^2 R_{\mathrm{l}}^2)}\Big). \tag{9.13}$$

Here*, $0 \leq \lambda \leq 1$, and, for the ideal HBT situation, $\lambda = 1$. Other geometric parametrizations have been considered, and also further interference terms between the geometric parameters in Eq. (9.13) have been introduced [272].

The interpretational situation in heavy-ion collisions is complicated by the finite lifetime, and the strong dynamic evolution of the particle-emitting source. Thus detailed interpretation of the observed correlations between the particles produced requires development of model-dependent understanding, and a considerable amount of effort continues to be devoted to the interpretation of the data. Generally, the following hypotheses are made regarding the source of particles:

* In this section λ is not a fugacity.

https://doi.org/10.1017/9781009290753.013 Published online by Cambridge University Press

1. emission of particles is chaotic;
2. correlated particles do not arise primarily from decay of resonances, though a strong resonance input is expected for pion correlations;
3. particles do not interact subsequent to strong-interaction freeze-out – corrections for Coulomb effects are often applied; and
4. kinematic correlations, e.g., conservation of energy–momentum, are of no relevance.

A considerable wealth of available experimental results leads to a few conclusions of relevance to the understanding of the reaction mechanisms operating in relativistic nuclear collisions.

- No evidence is found for a major expansion of the hadronic fireball, which would be required, e.g., for a (long-lived) mixed (HG/QGP) intermediate phase. The nuclear-collision geometry determines the size of the source for pions and kaons.
- The size of the particle source is similar though a bit smaller for strange (kaons) than it is for non-strange particles (pions). Thus the conditions for production of these rather different particles are surprisingly similar.
- There is a proportionality of the central hadron multiplicity yield to the geometric volume of the source.
- Evidence for the occurrence of transverse flow of the particle source is seen.

These results are consistent with a reaction picture in which the (deconfined) fireball expands and then rather suddenly disintegrates and hadronizes. In such a process even the momentum freeze-out of final-state particles occurs at a relatively early stage of the evolution of strongly interacting matter.

Figure 9.11, compiled by the STAR collaboration [18], shows the experimental results, i.e., parameters introduced in Eq. (9.13), as functions of the collision energy $\sqrt{s_{\mathrm{NN}}}$ for pion-intensity interferometry. These results of diverse experimental groups (see the top of the figure) are only compatible with a compact pion source being present at all reaction energies. While this is expected for the lower AGS energies, at which the fireball of nuclear matter is expected to have nuclear size, the actual slight decrease in size seen at the RHIC with $\sqrt{s_{\mathrm{NN}}} = 130$ GeV and CERN–SPS with $\sqrt{s_{\mathrm{NN}}} = 17$ GeV implies that, despite a rapid observed expansion of the fireball, there is even more sudden production of hadrons without an extended period of hadronization.

As a function of collision energy, we see in Fig. 9.11 that the parameter $\lambda \leq 1$ falls smoothly and rapidly from unity (the ideal expected value for an incoherent source) to about 0.5 at the RHIC; this decrease is attributed partially to an increase in the fraction of pions arising from hadron resonances at higher energies. λ is also affected by several experiment-specific

https://doi.org/10.1017/9781009290753.013 Published online by Cambridge University Press

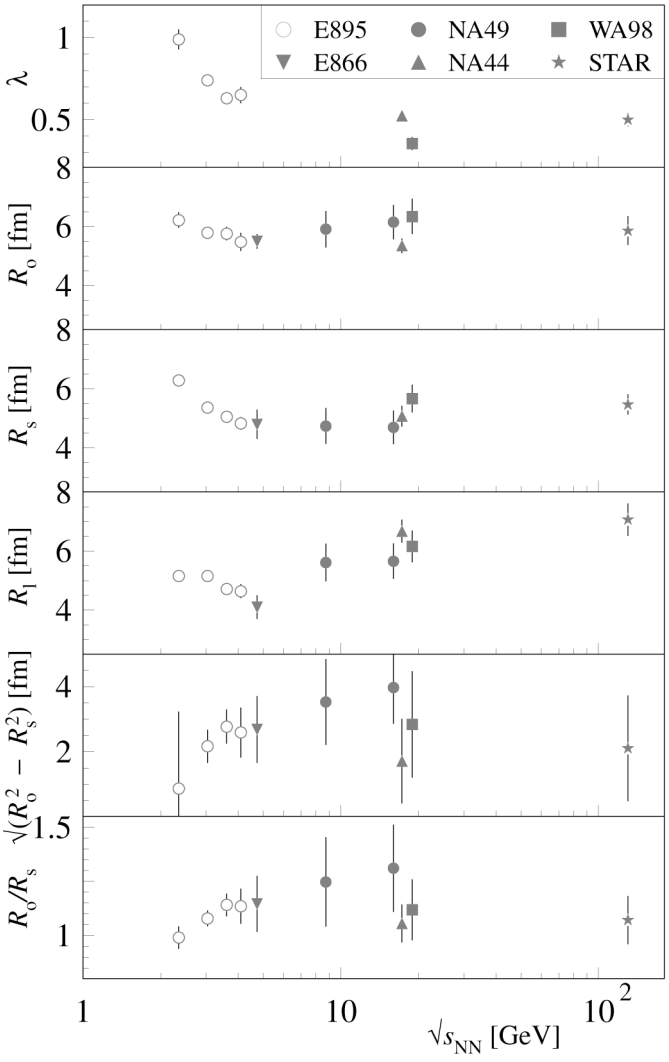

Fig. 9.11. Sizes of fireballs of excited nuclear matter derived from pion-correlation analysis, compilation and RHIC result by the STAR collaboration [18].

background effects and thus the physics of this behavior is not explored in depth.

The two parameters R_s and R_o correlate most directly to the geometry of the emitting source. This is illustrated in Fig. 9.12. The source of pions is here presumed to be a shallow surface structure; the 'out' direction is toward the eye of the observer. If the source is longitudinally deformed, and the observer is at a more transverse location, the effect is amplified

https://doi.org/10.1017/9781009290753.013 Published online by Cambridge University Press

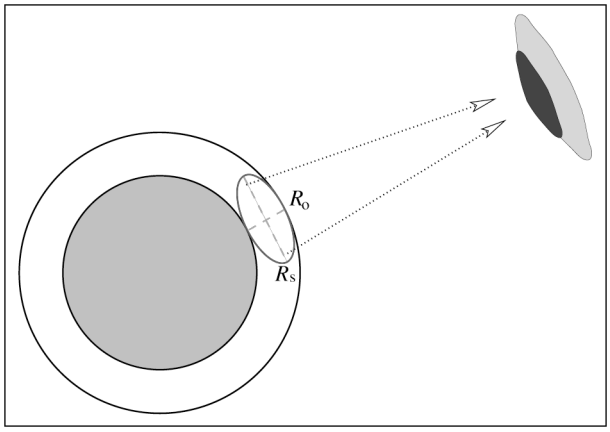

Fig. 9.12. Surface hadronization offers a possible explanation for why the HBT 'side' radius R_s can be larger than the radius measured out toward the eye of the observer, R_o.

by the geometry of the source. In contrast to this situation, simulations involving a long-lived phase of pion matter with pions originating from the volume of the fireball of dilute matter lead to $R_o/R_s > 1$. Experimental results, seen at the bottom of Fig. 9.11, deviate from this expectation most clearly at RHIC energies.

$R_o/R_s \simeq 1$ signals a rather short duration of pion production: one can show that, when spatio-temporal correlations vanish, $\delta \equiv \sqrt{R_o^2 - R_s^2}$ is a measure of the life span of the emitting source, which, as can also be seen in Fig. 9.11, is not as large as the equilibrium hadronization models require. The source volume $R_s^2 R_l$ is found to increase along with the total produced multiplicity of particles, as the centrality of the collision is varied at RHIC energies.

In addition to the overall behavior shown in Fig. 9.11, the STAR collaboration notes that the size parameters decrease significantly with increasing $m_\perp$ of particles. In that regard, the $m_\perp$ dependence at the RHIC is similar to, but stronger than that observed in central Pb–Pb collisions at the CERN–SPS facility. This suggests that the emission of hadrons at the RHIC is occurring from a more rapidly expanding surface source than is the emission at the SPS.

9.4 Production of transverse energy

So far, we have been describing production of hadronic particles and particle spectra. However, it is almost always simpler to measure the total 'flow' of energy contained in the various particles, rather than abundances

https://doi.org/10.1017/9781009290753.013 Published online by Cambridge University Press

of the many kinds of particles. The energy distribution can be used to determine the extent to which energy from the longitudinal motion of the colliding nuclei participates in the nuclear interaction. This is most easily done by considering the energy emitted in the transverse direction.

Since fragments of projectile and target contaminate the longitudinal flow, it is the transverse to the beam axis component of energy which is considered as a suitable measure of the amount of CM energy, Eq. (5.2), made available in the reaction for production of particles. Therefore, one studies the distribution of the energies of the particles, weighted by the sine of their angle θ_i with the beam axis (see Fig. 5.6), which is called the transverse energy,

$$E_\perp = \sum_i E_i \sin\theta_i. \tag{9.14}$$

The resulting distribution of transverse energy produced, $dE_\perp/d\theta$, as a function of the angle θ, can be converted into a distribution in pseudorapidity η by employing Eq. (5.25).

Experimentally, $dE_\perp/d\eta$ is determined with the help of a segmented calorimeter: particles entering a segment, covering a range of θ, deposit their energy, which is determined by exploiting various mechanisms of interaction of particles in matter – hence the name 'calorimeter' which derives from the name of a common heat measuring device. In fixed-target experiments, the laboratory-frame angle is not very large, see Fig. 5.7, and thus the calorimeter is typically located relatively far away, in front of the beam axis.

We show the transverse-energy-distribution data reported by the experiments WA98 [191] and NA49 [27], for 158A-GeV Pb–Pb (fixed-target) CERN experiments in Fig. 9.13. The key feature of this result is that there is a pronounced peak in the transverse energy distribution, slightly forward of the rapidity value $y = 2.9$. The shift in pseudorapidity distribution is a result of the definition of pseudorapidity; see Fig. 5.8 on page 88. This well-peaked distribution is consistent with the expectations based on the observed negative-particle distribution shown in Fig. 9.6.

The study of the transverse energy spectra has systematically been carried out for many systems and collision impact parameters, by numerous groups. It is worth noting that, for relatively small projectiles, doubling the mass of the projectile increases the geometric number of participants, in small-impact-parameter collisions, by approximately a factor $2^{2/3} \simeq 1.59$, corresponding to the increase in area of the impact surface on a large target. For example, an increase in $E_\perp$ by about a factor 1.6 was observed for the S–Au reactions relative to the O–Au reactions [201].

https://doi.org/10.1017/9781009290753.013 Published online by Cambridge University Press

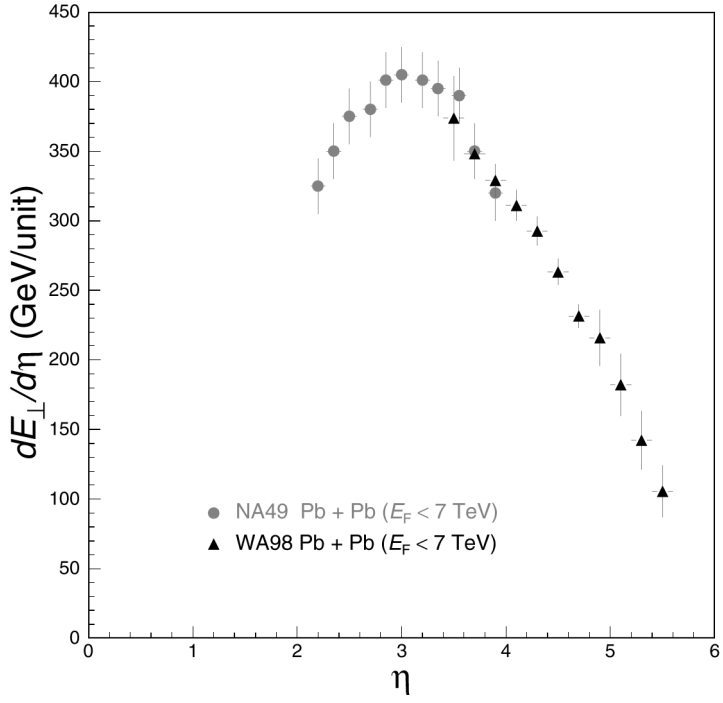

Fig. 9.13. The transverse energy distribution as a function of pseudorapidity for Pb–Pb fixed-target collisions at 158A GeV, with a central collision trigger. Combination of NA49 results [27] and WA98 results [191].

The three main trends observed on the SPS energy scale are

- the increase in the transverse energy with increasing mass of the colliding system,
- the increase in transverse energy with increasing energy, and
- the increase in the transverse energy with the number of participating nucleons, derived from the geometric centrality of the colliding nuclei; see section 5.2.

The measurement of transverse energy at the RHIC has produced a rather unexpected result, which we will discuss next.

9.5 RHIC results

With the first physics run at the RHIC, in 2000, a new domain of collision energy has been reached. These results were obtained at $\sqrt{s_{\mathrm{NN}}} = 130$ GeV and have produced some surprises when one compares them with SPS results. One is the discovery that the size of the fireball is barely different from that at the SPS, section 9.3, the other addresses the suppression

https://doi.org/10.1017/9781009290753.013 Published online by Cambridge University Press

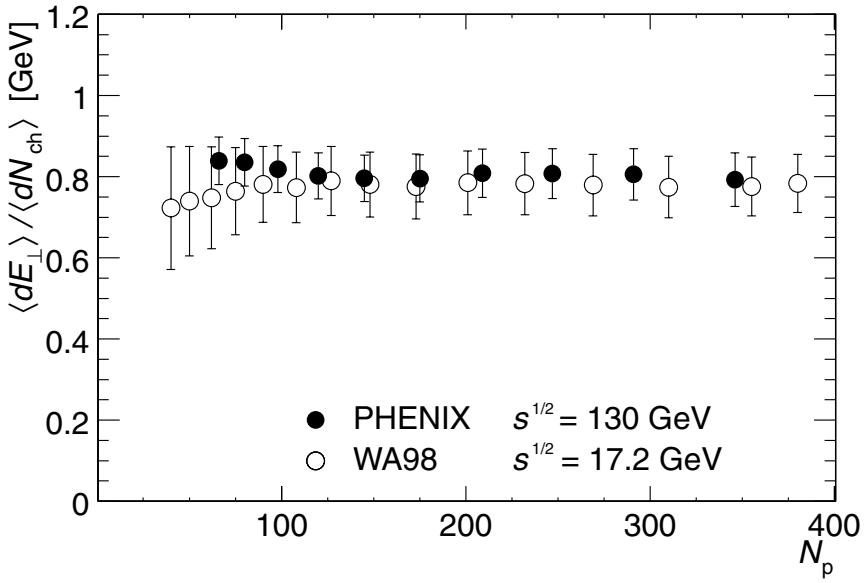

Fig. 9.14. The transverse energy per charged particle (solid dots) as a function of the number of participants at RHIC (PHENIX, 130 GeV) and at SPS (WA98, Pb–Pb fixed-target collisions at 158A GeV).

of hard parton production noted in section 8.4. In Fig. 9.14 we see the constancy of the transverse-energy yield per charged hadron produced.

Once the number of participants exceeds 100, there is no difference from the results we presented in Fig. 9.13 for the most central collisions, when results are expressed per participant, both PHENIX and WA98 results are shown in Fig. 9.14. This agreement between two different energy regimes is natural should the hadron-production mechanism at the RHIC and SPS be the same, as would be expected if a new state of matter were formed, hadronizing in both cases under similar conditions. The difference between the SPS and the RHIC is in the hadron-multiplicity yield, which is related to the total entropy available to hadronize.

There is more total transverse energy produced at the RHIC at central rapidity, than there is at the SPS, and this is seen on considering the pseudorapidity density of transverse energy per pair of participants, shown in Fig. 9.15. We note that the number of colliding pairs is half of all participants, i.e., in case of p–p reaction, there are two participants and one pair, and thus in this case the experimental data can be shown as measured.

We thus conclude that the extra deposition of energy per unit of rapidity at the RHIC is converted into extra hadronic particles, which explains the remarkable result we saw in Fig. 9.14. It will be most interesting to

https://doi.org/10.1017/9781009290753.013 Published online by Cambridge University Press

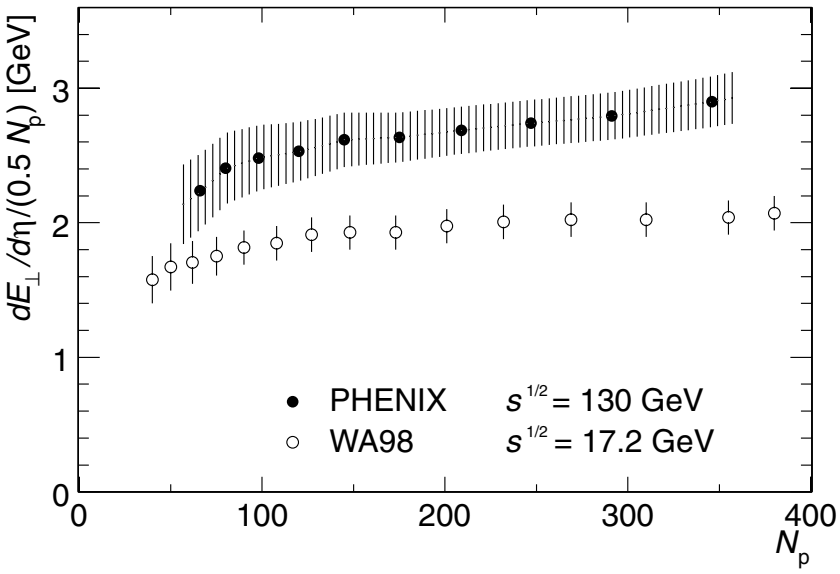

Fig. 9.15. The transverse-energy pseudorapidity density per pair of participants as a function of the number of participants, obtained at RHIC (PHENIX) and at SPS (WA98) [16].

see whether this trend continues in the near future; that is, whether, at the highest RHIC energy, $\sqrt{s_{\rm NN}} = 200$ GeV, the transverse energy per hadron produced will remain constant and only an increase in production of hadronic particles will be observed.

We now turn to the excitation function of hadron production (dependence on $\sqrt{s_{\rm NN}}$), and we include the first results at 200 GeV from RHIC. The central-rapidity charged-hadron yield per pair of participants is shown as a function of the collision energy $\sqrt{s_{\rm NN}}$ (on a logarithmic scale) in Fig. 9.16. We see three experimental heavy-ion-multiplicity yields at the RHIC: Au–Au results at $\sqrt{s_{\rm NN}} = 56$, 130, and 200 GeV (filled black data points) [50], CERN–SPS NA49 Pb–Pb results at $\sqrt{s_{\rm NN}} = 17.2 = 2 \times 8.6$ GeV and 4.3 GeV (open circles), and the low-energy AGS results. This is compared with p–$\bar{\rm p}$ inelastic-collision results of UA5 (CERN) and CDF (Fermilab). The interpolation line for the p–$\bar{\rm p}$ results defines reference yields used in Fig. 9.17. The importance of the RHIC results is clear, since without these one could argue that the top-energy SPS point is in agreement with the p–$\bar{\rm p}$ line, which, given RHIC results, we recognize to be near a crossing point of two very different types of behavior. We recall that some of these data are also shown in Fig. 9.7.

The maximum-energy result from the RHIC ($\sqrt{s_{\rm NN}} = 200$ GeV) falls on a nearly straight line, which begins near the intercept $\sqrt{s_{\rm NN}} = 1$ GeV,

https://doi.org/10.1017/9781009290753.013 Published online by Cambridge University Press

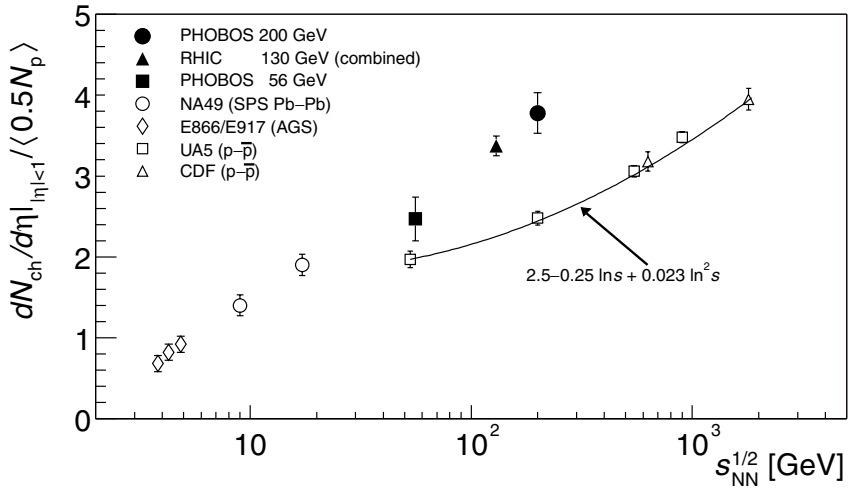

Fig. 9.16. The charged-hadron multiplicity per pair of participants at central rapidity as a function of $\sqrt{s_{\rm NN}}$, on a logarithmic display. Shown are results for the 6% most central Au–Au collisions at the RHIC (PHOBOS) at $\sqrt{s_{\rm NN}} = 56$, 130, and 200 GeV (filled black data), SPS Pb–Pb results (open circles), AGS results (open diamonds), along with the high-energy p–$\bar{\rm p}$ data (open squares and triangles), which are fitted to an empirical formula [50].

and follows within error all other experimental heavy-ion points. Thus, to a remarkable accuracy, the central-rapidity multiplicity in heavy-ion collisions is described by the empirical relation

$$\boxed{\frac{dN_{\rm ch}}{d\eta} = (1.6 \pm 0.1)\frac{1}{2} N_{\rm part}\ \log\left(\frac{\sqrt{s_{\rm NN}}}{\rm GeV}\right).} \tag{9.15}$$

The overall yield of particles produced is increasing faster than linearly with $\log \sqrt{s_{\rm NN}}$. However, the decrease in stopping just compensates for the increase in rapidity density, distributing the increase in particle yield over a wider range of (pseudo)rapidity. If this simple scaling, Eq. (9.15), were to continue to the LHC energy range, the rapidity density per participant would be 'only' 6–7 per pair of participants. For the 6% most central events, corresponding to $N_{\rm part} = 365$ in Pb–Pb interactions at the LHC, a relatively low $dN_{\rm ch}/d\eta \lesssim 2500$ charged particles yield per unit of pseudorapidity is thus expected, based on this simple extrapolation.

We now consider the charged particle yield at central rapidity, per participant pair. The dependence on the number of participants $N_{\rm part}$, shown in Fig. 9.17, (from the PHENIX collaboration) agrees with the results obtained by the PHOBOS collaborations [48, 281]. In Fig. 9.17, we also see to the left the UA5 p–$\bar{\rm p}$ ($\sqrt{s} = 130$ GeV) interpolated value. The periph-

https://doi.org/10.1017/9781009290753.013 Published online by Cambridge University Press

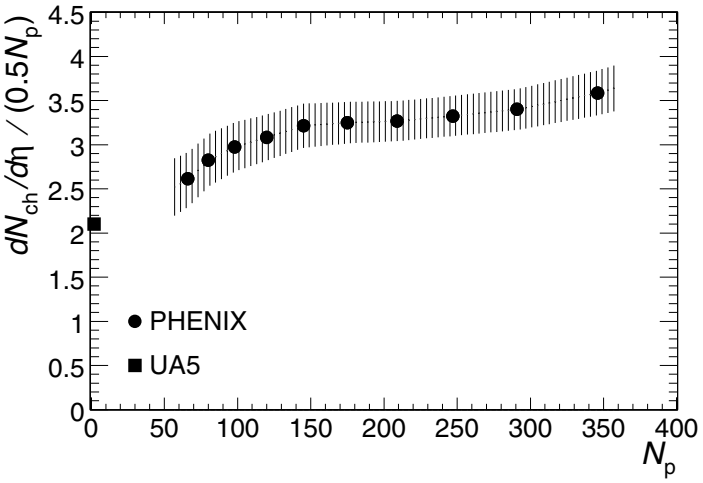

Fig. 9.17. Production of charged hadrons at central rapidity in Au–Au collisions at $\sqrt{s_{\rm NN}} = 130A$ GeV, obtained at various collision centralities, and presented per pair of participants as a function of the number of participants (solid circles, the uncertainty is shaded) [281]. The solid square is the interpolated result from UA5 p–$\bar{\rm p}$.

eral yield in Au–Au interactions for 50–100 participants extrapolates well to this point. A slight increase in the specific yield of charged hadrons is noted for the most central collision. Overall, an increase of 50% in specific yield of hadrons per participant is observed on comparing N–N with p–$\bar{\rm p}$ reactions. This very characteristic behavior allows discrimination between models of hadron production. This is a topic in rapid evolution which we will not further pursue at this time.

The primary reason to move to the highest accessible nuclear collision energies is the desire to create a matter–antimatter-symmetric state of dense matter akin to the conditions present in the early Universe. A baryon-free QGP state should be accessible in LHC experiments. However, at $\sqrt{s} = 130A$ GeV at the RHIC, considerable matter–antimatter asymmetry is still observed. A measure of the baryon content is obtained by inspecting the central-rapidity antiproton-to-proton ratio $\bar{\rm p}$/p. In Fig. 9.18, devised by the STAR collaboration [19], to the right, we see that, in the mid-rapidity region, this ratio is appreciably different from unity. In view of the systematic behavior seen in the p–p interactions (open symbols), this is not unexpected, though there was some hope that a rapid onset of longitudinal expansion of matter could precipitate the creation of the baryon-free region at the RHIC.

The low-energy 'AGS' point is showing the production threshold, the observed small ratio is not visible on the scale of the figure. We note

https://doi.org/10.1017/9781009290753.013 Published online by Cambridge University Press

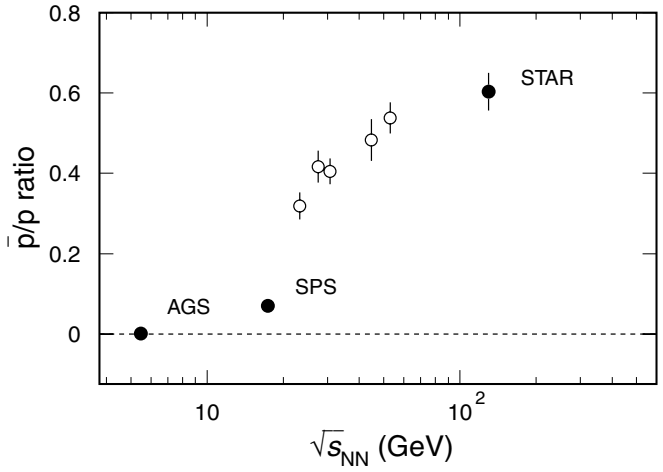

Fig. 9.18. The mid-rapidity antiproton-to-proton ratio ($\bar{p}/p$) measured in central heavy-ion collisions (filled symbols) and p–p collisions (open symbols).

a marked increase of the antimatter-to-matter ratio on going from SPS to RHIC energies. As expected, the conversion of kinetic energy available in the interaction into hadron multiplicity, and here specifically antibaryons, is more effective in A–A reactions at RHIC energies than it is in p–p and even matter–antimatter p–$\bar{p}$ interactions, as can be seen in Fig. 9.16.

The (pseudo)rapidity shape of the charged-particle distribution, see Fig. 9.19, as measured by the PHOBOS collaboration, displays a flat top, as could be expected in the punch-through case, see Fig. 5.2 on page 74. The presence of a slight central dip could be in part due to pseudorapidity being used as a variable, see section 8.1. For the most central 3% collisions one finds a charged-hadron multiplicity of $\langle h^+ + h^- \rangle = 4100 \pm 100\,(\text{statistical}) \pm 400\,(\text{systematic})$, within the interval $|\eta| \leq 5.4$ [230]. This is nearly a 3-fold increase compared with the SPS yield (for h^- see Fig. 9.6), while the collision CM energy is 7.5-fold higher. This implies that a high fraction of the collision energy is available for production of particles at RHIC energies. This fraction is less than for the SPS due to greater transparency at higher energy.

The charged-hadron rapidity distributions, shown in Fig. 9.19, are seen to fall within the rapidity gap between projectile and target rapidities. We see again the physics motivation to desire a rapidity separation, which is available at the RHIC collider: particles produced at central rapidity cannot be confounded with contributions from fragmentation of the projectile and target.

https://doi.org/10.1017/9781009290753.013 Published online by Cambridge University Press

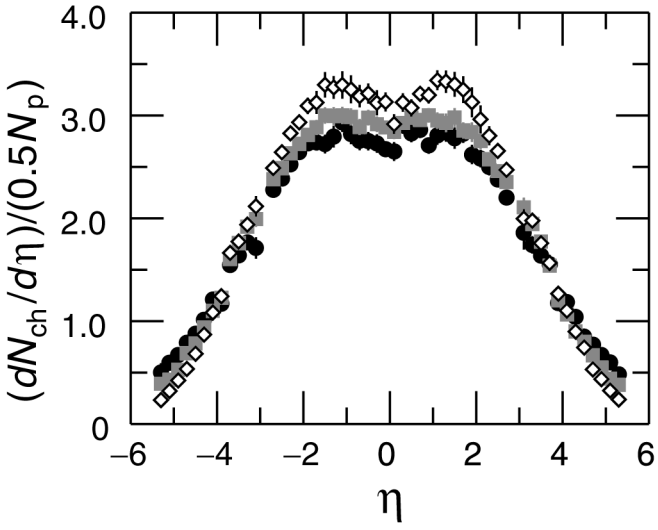

Fig. 9.19. The rapidity distribution of charged hadrons in Au–Au collisions at $\sqrt{s_{NN}} = 130A$ GeV obtained at various collision centralities implying numbers of participants $\langle N \rangle$ =102, 216, and 354 for open circles, squares, and diamonds, respectively. Phobos collaboration [230].

Turning briefly to strangeness we note that the STAR experiment reported the result

$$\left.\frac{dN_{K^+}}{dy}\right|_{y=0} = 35 \pm 3.5, \quad \left.\frac{dN_{K^-}}{dy}\right|_{y=0} = 30 \pm 3.$$

Allowing for strangeness in neutral kaons and hyperons

$$\left.\frac{d\bar{s}}{dy}\right|_{y=0} = \left.\frac{ds}{dy}\right|_{y=0} > 100.$$

This very large abundance of strangeness has to be compared with the yield of non-strange hadrons:

$$\frac{d\pi^+}{dy} \simeq \frac{d\pi^-}{dy} \simeq 235.$$

The primary number of mesons is ≃175, considering resonance cascading, see section 7.3. Strangeness is thus reaching near symmetry with light flavors. We will return to a full analysis of this interesting subject in section 19.4.

It is quite clear, given the RHIC results, that the nucleus–nucleus collisions differ substantially from elementary hadronic collisions such as p–p and p–$\bar{p}$ in their hadron-production efficiency. The conditions reached at

https://doi.org/10.1017/9781009290753.013 Published online by Cambridge University Press

the RHIC are clearly more extreme than at SPS. The $\sqrt{s_{\rm NN}} = 130$ GeV, RHIC central-rapidity hadron yield is about 40% higher at 7.5-fold higher CM collision energy than that seen at SPS, as can be seen in Fig. 9.16. Inspecting Eq. (7.27) and noting that τ_0, the initial thermal equilibration time, is most likely shorter at the RHIC than it is at the SPS, we conclude that the initial entropy density is at least 40%, and probably more than that, greater than that at the SPS. Along with the entropy density, given that the energy per particle seen at the RHIC is similar to results observed at CERN, see Fig. 9.14, we expect a similar enhancement of initial energy density reached during the 2000 RHIC run at 130A GeV, compared with CERN top-energy results.

Can we estimate more precisely the initial energy density produced at the RHIC? In order to convert Eq. (7.27) into a relation for the initial energy density, we can use $E/S = \epsilon/\sigma$, the energy per unit entropy available. For a relativistic (massless) gas with $P = \epsilon/3$ at negligible baryon density, the Gibbs–Duham relation, Eq. (10.30), implies that $\epsilon_0 = \frac{3}{4} T_0 \sigma_0$. Thus, Eq. (7.27) also means that

$$\epsilon_0 = \frac{A^{1/3}}{\pi (1.2\,\mathrm{fm})^2} \frac{T_0}{\tau_0} \frac{9}{4} \frac{dN_{\rm ch}/(0.5A)}{dy}. \tag{9.16}$$

This slightly unusual form Eq. (9.16), as stated here, shows that the initial energy density, apart from an increase due to an enhancement in multiplicity density, also increases at RHIC compared to SPS due to two likely changes in the initial condition: a shortening of the initial thermalization time τ_0 for the more dense initial state formed at the higher RHIC energy, and also an associated increase of the initial temperature T_0 at which thermalization has occurred. Of course, it is very difficult to pin down quantitatively these two contributions to the initial increase in energy density. On the other hand, combined they could be as important as the increase in the energy density due to an increase in the final state particle multiplicity.

In order to arrive at an estimate for ϵ_0, we take $T_0 = 300$ MeV and $\tau_0 = 1$ fm, and, for $A = 350$, we use the result seen in Fig. 9.17, $dN_{\rm ch}/(0.5A) = 3.5$. We obtain $\epsilon_0 = 16$ GeV fm^{-3}. Lattice calculations seen in Fig. 15.3 on page 300 suggest [159]: $\epsilon_0 \simeq 11 T_0^4$, which yields for $\epsilon_0 = 16$ GeV fm^{-3} a temperature $T_0 = 325$ MeV. Given our ignorance of the value of τ_0 and remaining uncertainties in lattice studies of QGP equations of state, we estimate that the energy density and temperature reached at the RHIC are $\epsilon_0 \simeq 15$–20 GeV fm^{-3} and $T_0 \simeq 320$–330 MeV $\geq 2T_{\rm c}$, where $T_{\rm c}$, the critical temperature for deconfinement, is estimated to be about 160 MeV [159]; section 15.5.

The 'Bjørken energy formula' used often in such estimates arises from Eq. (9.16) by the substitution $3T_0 N_{\rm ch}/(0.5A) \to \langle E \rangle$. $\langle E \rangle$ is the mean

https://doi.org/10.1017/9781009290753.013 Published online by Cambridge University Press

energy per pair of participants,

$$\varepsilon_0 \simeq \frac{A^{1/3}}{\pi(1.2\,\mathrm{fm})^2\tau_0}\frac{d\langle E_\perp\rangle}{d\eta}. \tag{9.17}$$

This expression leads to a lower energy-density estimate, since it does not account for the factor T_0/T_f implicitly present in Eq. (9.16) and omitted in Eq. (9.17).

https://doi.org/10.1017/9781009290753.013 Published online by Cambridge University Press